

Eigenstate structures around a hyperbolic point

S. Nonnenmacher and A. Voros

CEA–Saclay, Service de Physique Théorique
F-91191 Gif-sur-Yvette CEDEX (France)

February 5, 2008

Abstract

Using coherent-state representations of quantum mechanics (Bargmann, Husimi, and stellar representations), we describe analytically the phase-space structure of the general eigenstates corresponding to a 1-dimensional bilinear hyperbolic Hamiltonian, $H = pq$ or equivalently $H = \frac{1}{2}(P^2 - Q^2)$. Their semi-classical behaviour is discussed for eigenvalues either near or away from the separatrix energy $\{H = 0\}$, especially in the phase-space vicinity of the saddle-point $(q, p) = (0, 0)$.

1 Introduction

Semiclassical theory, and the quantum–classical correspondence, are still incompletely understood at the level of long-time or invariant structures, especially when the classical dynamics shows exponential sensitivity to initial conditions (instability, or positive Lyapunov exponents).

We have therefore selected a simple 1-d system, the dilation operator which quantizes the classical linear hyperbolic Hamiltonian $H(q, p) = qp$, and collected some detailed analytical properties of its eigenstates. Elementary as this quantum Hamiltonian may be, seemingly unreported expressions for its eigenstates are given here, precisely within the coherent-state (Bargmann or Husimi) formulations where the semiclassical behaviour ($\hbar \rightarrow 0$ asymptotics) of quantum states is best seen.

Formulae for this “dilator” should be useful tools to probe quantum phenomena linked to unstable (here, hyperbolic) classical dynamics. Here are two actively studied examples involving this Hamiltonian:

- in one dimension, classical hyperbolic dynamics takes place near a saddle-point (assuming it is generic, i.e., isolated and nondegenerate); then it is locally equivalent to $H = pq$ in suitable canonical coordinates, i.e, the classical dilator is the local normal form for this class of problems. At the quantum level, 1-d saddle-points also challenge semiclassical analysis: like energy minima, they correspond to

critical energy values (i.e., the phase-space velocity vanishes); semiclassical analysis is fundamentally harder at critical than at regular energy values (where simple WKB theory works), but saddle-points are even harder to understand than minima and their study has expanded more recently [1, 2, 3].

- in higher dimensions, the search for quantum manifestations of unstable classical motion forms one facet of the “quantum chaos” problem. For instance, the role and imprint of unstable periodic orbits upon quantum dynamics remain actively debated issues. It is known that they influence both the quantum bound state energy spectrum (through trace formulas) and wave functions (through scarring). More specifically, the (stable) orbits of elliptic type generate quantization formulas and quasimode constructions in a consistent way. In chaotic systems, by contrast, trace formulas diverge and scarring occurs rather unpredictably, so that periodic orbits (now unstable) have incompletely assessed quantum effects; nevertheless, an essential role must still go to their linearized classical dynamics, which is of hyperbolic type hence generated by linear dilator(s).

Fully chaotic behaviour, a combination of global instability plus ergodic recurrence, cannot however be captured by integrable models; therefore, the place of the 1-d dilator eigenfunctions in quantum structures corresponding to fully chaotic dynamics remains to be further studied. At present, these eigenfunctions should primarily find use as microlocal models for general 1-d eigenstates near saddle-points (and for separatrix eigenstates in higher-dimensional integrable systems, by extension).

2 Coherent-state representations

2.1 Bargmann representation

The Bargmann representation [4] is a particular coherent-state representation of quantum wave-functions [5, 6, 7] in terms of entire functions. Although it can be defined in any dimension, we will just use it for 1-dimensional problems; it then transforms Schrödinger wave-functions $\psi(q)$ defined over the whole real line into entire functions $\psi(z)$ of a complex variable z , as

$$\psi(z) = \langle z|\psi \rangle = \frac{1}{(\pi\hbar)^{1/4}} \int_{\mathbb{R}} e^{\frac{1}{\hbar}(-\frac{1}{2}(z^2+q'^2)+\sqrt{2}zq')} \psi(q') dq'. \quad (1)$$

Here $|z\rangle$ denotes a (Weyl) coherent state localized at the phase space point (q, p) where $z = 2^{-1/2}(q - ip)$, and satisfying $\langle z|z'\rangle = e^{z\bar{z}'/\hbar}$; i.e. these coherent states are not mutually orthogonal, and their normalization is not $\langle z|z\rangle = 1$, allowing instead the bra vector $\langle z|$ to be a holomorphic function of its label z . On the other hand, a closure formula exists which makes the Bargmann transform invertible,

$$\mathbb{1} = \int_{\mathbb{C}} \frac{d\Re(z)d\Im(z)}{\pi\hbar} e^{-z\bar{z}/\hbar} |z\rangle\langle z|. \quad (2)$$

The Bargmann transformation maps ordinary square-integrable wave-functions into a Hilbert space of entire functions of order ≤ 2 . We will however mostly

deal with generalized wave-functions $\psi(q)$, which are not L^2 but only tempered distributions. They can then still be Bargmann-transformed by the integral formula (1), and into entire functions of order ≤ 2 as before, now bounded as

$$|\psi(z)| \leq c(1 + |z|^2)^N e^{\frac{|z|^2}{2\hbar}} \quad \text{for some } N. \quad (3)$$

This in turn constrains the distribution of their zeros [8]: the counting function

$$n(r) = \#\{\text{zeros } z_m \text{ of } \psi(z) \text{ s.t. } |z_m| \leq r\} \quad (4)$$

(zeros will be always counted with their multiplicities) verifies

$$\limsup_{r \rightarrow \infty} \frac{n(r)}{r^2} \leq \frac{e}{\hbar}. \quad (5)$$

It follows that a Bargmann function admits a canonical Hadamard representation as an (in)finite product over its zeros,

$$\psi(z) = e^{p(z)} z^{n(0)} \prod_{z_m \neq 0} \left(1 - \frac{z}{z_m}\right) \exp\left(\frac{z}{z_m} + \frac{1}{2}\left(\frac{z}{z_m}\right)^2\right) \quad (6)$$

where $p(z) = \hbar^{-1}(a_2 z^2 + a_1 z + a_0)$, with moreover $|a_2| \leq 1/2$; the integer $n(0) \geq 0$ is the multiplicity of $z = 0$ as a zero of $\psi(z)$. This decomposition shows that the wave-function is completely determined by the knowledge of all the Bargmann zeros (with their multiplicities) plus three coefficients a_2, a_1 , and a_0 (which only fixes a constant factor).

When the Hamiltonian is a polynomial (or more generally an analytic function) in the variables (q, p) , it can be useful to express its quantum version as a pseudo-differential operator acting on the Bargmann function [4], using the rules

$$\begin{aligned} a^\dagger &= \frac{\hat{q} - i\hat{p}}{\sqrt{2}} & (\text{creation operator}) & \rightarrow \text{multiplication by } z \\ a &= \frac{\hat{q} + i\hat{p}}{\sqrt{2}} & (\text{annihilation operator}) & \rightarrow \hbar \frac{\partial}{\partial z}. \end{aligned} \quad (7)$$

2.2 Husimi representation

An alternative point of interest lies in certain semi-classical densities on phase space associated to wave-functions. In particular, the Wigner function is defined as

$$\mathcal{W}_\psi(q, p) = (2\pi\hbar)^{-1} \int_{\mathbb{R}} \psi(q - r/2) \overline{\psi}(q + r/2) e^{ipr/\hbar} dr \quad (8)$$

and the Husimi function [9] as the convolution of the Wigner function with a phase-space Gaussian,

$$\mathcal{H}_\psi(q, p) = (\pi\hbar)^{-1} \int_{\mathbb{R}^2} \mathcal{W}_\psi(q', p') e^{-[(q-q')^2 + (p-p')^2]/\hbar} dq' dp'. \quad (9)$$

The Wigner representation has greater symmetry (invariance under all linear symplectic transformations), but Wigner functions show a much less local semiclassical behaviour: they tend to display huge nonphysical oscillations, which must be averaged out to reveal any interesting limiting effects. In the Husimi functions, the spurious oscillations get precisely damped so as to unravel the actual phase-space concentration of the semiclassical measures, but at the expense of reducing the invariance group. The Husimi function is equivalently given by

$$\mathcal{H}_\psi(z, \bar{z}) = \frac{\langle z|\psi\rangle\langle\psi|z\rangle}{\langle z|z\rangle} = |\psi(z)|^2 e^{-z\bar{z}/\hbar} \quad (10)$$

hence it constitutes the density of a positive measure on the phase space; for the scattering-like eigenfunctions to be studied here, this measure will not be normalizable. (For a normalized state, it is a probability measure thanks to the closure formula (2).)

It is interesting to study how the Husimi measure of an eigenfunction behaves as $\hbar \rightarrow 0$. For an energy away from the separatrix, a standard theorem states that this measure concentrates on the energy surface, with a Gaussian transversal profile [10, 11, 12]. For energies close to a separatrix, careful analyses were performed in [1, 2, 3]. Our aim here is to select a simple tractable case, namely the eigenfunctions of the linear hyperbolic Hamiltonian [13], and to carry further its description by means of the Bargmann representation, using eq. (10) to derive the Husimi density as a by-product.

2.3 Stellar representation

According to the factorized representation (6), 1-d quantum wavefunctions can be essentially parametrized in a phase-space geometry by the distribution of their Bargmann zeros which, by eq. (10), is also the pattern of zeros for the Husimi density itself; it thus constitutes a complementary viewpoint to the previous emphasis put on the high-density behaviour of the Husimi function. We refer to this “reduced” description of a wavefunction by a discrete cloud of phase-space points as a stellar representation. It puts quantum mechanics in a new perspective [14, 15, 16], but calls for a finer understanding of both dynamical and asymptotic properties of Bargmann zeros if new results are to be awaited through eq. (6). Consequently, our subsequent analysis of “toy” eigenfunctions will largely deal with explicit behaviours of their Bargmann zeros.

3 Description of the framework

3.1 The linear hyperbolic Hamiltonian

The classical 1-dimensional Hamiltonian of linear dilation is $H(q, p) = pq$, which is also equivalent to the scattering Hamiltonian $H = \frac{1}{2}(P^2 - Q^2)$ upon a symplectic

rotation of the coordinates by $\pi/4$ according to

$$q = \frac{P+Q}{\sqrt{2}}, \quad p = \frac{P-Q}{\sqrt{2}}. \quad (11)$$

A classical trajectory at any energy $E \neq 0$ is a hyperbola branch,

$$q(t) = q_0 e^t, \quad p(t) = p_0 e^{-t} \quad \text{with } E = p_0 q_0 \quad (12)$$

whereas the $E = 0$ set is a separatrix, made of a stable manifold $\{p = 0\}$, an unstable manifold $\{q = 0\}$, and the hyperbolic fixed point $(0, 0)$.

We study eigenfunctions of the operator obtained by Weyl quantization, namely $\hat{H} = \frac{\hbar}{i}(q \frac{d}{dq} + \frac{1}{2})$. This quantum Hamiltonian admits two independent stationary wave-functions for any real energy E :

$$\psi_{\pm}^E = K \theta(\pm q) e^{(i\frac{E}{\hbar} - \frac{1}{2}) \log |q|} \quad (13)$$

where $\theta(q)$ is the Heaviside step function; $K \neq 0$ is a complex constant (having no preferred value, since the solutions are not square-integrable). Microlocally, each of these wavefunctions is supported by the lagrangian manifolds $\Lambda_{\pm}^E = \{pq = E, \pm q > 0\}$, i.e. half of the E -energy surface [1].

In order to obtain more semi-classical information, we will use the Bargmann representation. For instance,

$$\langle z | \psi_+^E \rangle = \psi_+^E(z) = \frac{K}{(\pi \hbar)^{1/4}} \int_0^\infty e^{\frac{1}{\hbar}(-\frac{1}{2}(z^2 + q'^2) + \sqrt{2}zq' + iE \log q')} \frac{1}{\sqrt{q'}} dq' \quad (14)$$

and we have of course

$$\psi_-^E(z) = \psi_+^E(-z); \quad \psi_{\pm}^{-E}(z) = \overline{\psi_{\pm}^E(\bar{z})}. \quad (15)$$

Our aim in this paper is to describe the general eigenfunction of energy E in this representation: up to a global (removable) constant factor, it reads as $\psi_{\lambda}^E(z) = \psi_+^E(z) + \lambda \psi_-^E(z)$, for any complex projective parameter λ , i.e. $\lambda \in \overline{\mathbb{C}} = \mathbb{C} \cup \{\infty\}$. We can immediately restrict attention to $E \geq 0$ due to the second of eqs. (15). We will be particularly interested, on the one hand, in the global profile of these functions, and on the other hand, in the position of their zeros because these form the main skeleton of the Hadamard product representation (6) [14].

The motivation is to better describe the eigenfunctions of a general 1-d Hamiltonian for eigenvalues close to a classical saddle-point energy value. Such an eigenfunction cannot be simply of WKB form near the saddle-point; instead, it should be microlocally modeled by an eigenvector ψ_{λ}^E of the dilation operator \hat{H} near $(q, p) = 0$ with $E \approx 0$ (up to straightforward displacements, in phase space and in energy). Thus, in a Bargmann representation, the eigenfunction near $z = 0$ ought to behave like $\psi_{\lambda}^E(z)$ for some λ , which is the one quantity whose actual value is determined by global features of the solution. (In particular, for a parity-symmetric 1-d Hamiltonian and for a saddle-point located at the symmetry center, only even or odd solutions ever come into play; hence parity conservation preselects the two eigenfunctions of \hat{H} with the special values $\lambda = +1$ and -1 respectively.)

3.2 Main analytical results

The functions $\psi_\lambda^E(z)$ are also solutions of the Schrödinger equation written in the Bargmann representation,

$$\frac{i}{2} \left(-\hbar^2 \frac{d^2}{dz^2} + z^2 \right) \psi^E(z) = E \psi^E(z). \quad (16)$$

It is convenient to use the rotated variables Q, P and $Z = 2^{-1/2}(Q - iP) = z e^{-i\pi/4}$ in parallel with q, p , and z . In those variables the quantum Hamiltonian reads as the quadratic-barrier Schrödinger operator $\hat{H} = \frac{1}{2}(-\hbar^2 d^2/dQ^2 - Q^2)$. Its Bargmann transform happens to be exactly the same operator in the Z variable, simply continued over the whole complex plane, so that the eigenfunction equation can also be written as

$$\frac{1}{2} \left(-\hbar^2 \frac{d^2}{dZ^2} - Z^2 \right) \Psi^E(Z) = E \Psi^E(Z). \quad (17)$$

At the same time, the Bargmann representations obtained from q and Q are equivalent under a simple complex rotation,

$$\Psi(Z) = \psi(z) \quad \text{with } Z = z e^{-i\pi/4}. \quad (18)$$

Consequently, as a main first result, the above solutions are directly related to the parabolic cylinder functions $D_\nu(y)$, defined for example in [17]. As a matter of fact, we have :

$$\Psi_\pm^E(Z) = \psi_\pm^E(z) = K \frac{\hbar^{iE/2\hbar}}{\pi^{1/4}} \Gamma\left(\frac{1}{2} + \frac{iE}{\hbar}\right) D_{-\frac{1}{2} - \frac{iE}{\hbar}}\left(\mp \sqrt{\frac{2}{\hbar}} z\right). \quad (19)$$

Up to rescaling, the Bargmann eigenfunction $\psi_\lambda^E(z)$ is then simply a linear combination of known functions, $[\lambda D_\nu(y) + D_\nu(-y)]$ with the notations $y = \sqrt{2/\hbar} z$ and $\nu = -\frac{1}{2} - i\frac{E}{\hbar}$.

The situation simplifies even further on the separatrix $E = 0$, where parabolic cylinder functions reduce to Bessel functions, as

$$\begin{aligned} D_{-1/2}(y) &= \left((2\pi)^{-1} y\right)^{1/2} K_{1/4}\left(y^2/4\right) \\ D_{-1/2}(y) + D_{-1/2}(-y) &= e^{+i\pi/8} (\pi y)^{1/2} J_{-1/4}\left(iy^2/4\right) \\ -D_{-1/2}(y) + D_{-1/2}(-y) &= e^{-i\pi/8} (\pi y)^{1/2} J_{1/4}\left(iy^2/4\right). \end{aligned} \quad (20)$$

By virtue of eq. (10), eqs. (19) and (20) yield the Husimi densities in closed form, for all eigenfunctions; e.g., for $\psi_+^E(z)$ and $\Psi_{\pm 1}^0(Z)$ respectively,

$$\begin{aligned} \mathcal{H}_+^E(z, \bar{z}) &= \frac{|K|^2 \sqrt{\pi}}{\cosh(\pi E/\hbar)} |D_{-\frac{1}{2} - i\frac{E}{\hbar}}(-\sqrt{2/\hbar} z)|^2 e^{-z\bar{z}/\hbar} \\ \mathcal{H}_{\pm 1}^0(Z, \bar{Z}) &= |K|^2 \sqrt{2\pi^3/\hbar} |Z| |J_{\mp 1/4}(Z^2/2\hbar)|^2 e^{-Z\bar{Z}/\hbar}. \end{aligned} \quad (21)$$

This is an interesting extension of earlier similar formulas for the Wigner functions; e.g., for ψ_+^E , [18]

$$\begin{aligned}\mathcal{W}_+^E(q, p) &= \frac{|K|^2}{\hbar \cosh(\pi E/\hbar)} \theta(q) e^{2ipq/\hbar} {}_1F_1\left(\frac{1}{2} + \frac{iE}{\hbar}; 1; -4ipq/\hbar\right) \\ \mathcal{W}_+^{E=0}(q, p) &= |K|^2 \hbar^{-1} \theta(q) J_0(4ipq/\hbar)\end{aligned}\quad (22)$$

where ${}_1F_1(-\nu; 1; x) \propto L_\nu(x)$ (Laguerre functions). These expressions are specially simple (constant along connected orbits) because the Wigner representation is exactly \hat{H} -invariant under the symplectic evolution generated by the bilinear Hamiltonian H . Inversely, coherent-state representations can never preserve such a dynamical invariance of hyperbolic type, hence closed-form results like (21) are necessarily more intricate than their Wigner counterparts and not simply transferable therefrom.

Fig. 1 shows contour plots for some of those Husimi densities, all with the normalizations $K = \hbar = 1$. The first example ($\mathcal{H}_+^E(z, \bar{z})$ for $E = +1$) is plotted twice: once with equally spaced contour levels starting from zero (linear scale), and once with contour levels in a geometric progression decreasing from the maximum (logarithmic scale). The linear plot emphasizes the high-density modulations which control the measure concentration of the Husimi density; the logarithmic plot reveals the subdominant structures and especially the locations of the zeros z_m which determine the Hadamard parametrization. For the parabolic cylinder function itself as an example, the factorization formula (6) specifically gives

$$\begin{aligned}D_\nu(z) &= e^{p(z)} \prod_{z_m \neq 0} \left(1 - \frac{z}{z_m}\right) \exp\left(\frac{z}{z_m} + \frac{1}{2}\left(\frac{z}{z_m}\right)^2\right), \\ p(y) &\equiv \log D_\nu(0) + (\log D_\nu)'(0) y + (\log D_\nu)''(0) y^2/2 \\ &= -\log \frac{\Gamma(\frac{1-\nu}{2})}{2^{\nu/2} \sqrt{\pi}} - \sqrt{2} \frac{\Gamma(\frac{1-\nu}{2})}{\Gamma(-\frac{\nu}{2})} y - \left(\frac{\nu}{2} + \frac{1}{4} + \left[\frac{\Gamma(\frac{1-\nu}{2})}{\Gamma(-\frac{\nu}{2})}\right]^2\right) y^2.\end{aligned}\quad (23)$$

In order to save figure space, we do not provide the log-plots used to locate the zeros for the other Husimi densities but only their linear contour plots, with the zeros superimposed as small dots. (The same uniform contour level spacing is used throughout to make comparisons easier.)

4 Asymptotic expansions

We can then rely upon the known asymptotic properties of the $D_\nu(y)$, which follow from the integral representation (14), to investigate two asymptotic regimes for the eigenfunctions of \hat{H} . Firstly, when E/\hbar is kept finite, the asymptotic expansions will be valid in the limit $y \rightarrow \infty$; this corresponds to eigenenergies very close to the classical separatrix energy $E = 0$. Secondly, if we fix the energy E at a non-vanishing value and let $\hbar \rightarrow 0$, we have to use a different type of asymptotics, namely usual WKB expansions.

4.1 Energies close to zero

We use the expansions for $D_\nu(y)$ when $|y| \rightarrow \infty$ [17] at fixed ν , which are obtained from integral representations using Watson's lemma, and take different forms in various angular sectors,

$$\begin{aligned}
-\frac{\pi}{2} < \arg(y) < +\frac{\pi}{2} & : \quad D_\nu(y) \sim y^\nu e^{-y^2/4} \sum_{n \geq 0} \frac{\Gamma(2n - \nu)}{n! \Gamma(-\nu)} \frac{1}{(-2y^2)^n} \sim y^\nu e^{-y^2/4} (1 + O(y^{-2})) \quad (24) \\
-\pi < \arg(y) < -\frac{\pi}{2} & : \quad D_\nu(y) \sim y^\nu e^{-y^2/4} (1 + O(y^{-2})) - \frac{\sqrt{2\pi}}{\Gamma(-\nu)} e^{-i\nu\pi} y^{-\nu-1} e^{y^2/4} (1 + O(y^{-2})) \\
+\frac{\pi}{2} < \arg(y) < +\pi & : \quad D_\nu(y) \sim y^\nu e^{-y^2/4} (1 + O(y^{-2})) - \frac{\sqrt{2\pi}}{\Gamma(-\nu)} e^{i\nu\pi} y^{-\nu-1} e^{y^2/4} (1 + O(y^{-2})).
\end{aligned}$$

The sectors are specified here as non-overlapping and bounded by Stokes lines, i.e. curves of maximal dominance of one exponential factor over the other. (Each asymptotic expansion actually persists in a larger sector overlapping with its neighbours, but this extension will not be of use here.) The above expansions are valid for $|y| \rightarrow \infty$ within each sector and provide approximations to the shape of the eigenfunctions and the positions of their zeros for large $|y|$; we will use them to leading order only (up to $O(y^{-2})$ terms). For the general eigenfunction $\psi_\lambda^E \propto [\lambda D_\nu(y) + D_\nu(-y)]$, eqs. (24) straightforwardly generate four different expansions in the four z -plane quadrants S_j , $j = 0, 1, 2, 3$ (named anticlockwise from $S_0 = \{0 < \arg z < \pi/2\}$).

4.2 WKB expansions for a fixed non-vanishing energy

The previous expansions are inapplicable when $\hbar \rightarrow 0$ with the classical energy kept fixed at a non-zero value (in the following we will suppose $E > 0$). In this regime, we have to use WKB-type expansions instead. These can be obtained from the integral representations of the solutions (14), by performing saddle-point approximations; equivalently, they can be found directly from the Schrödinger equation written in Bargmann variables (17). We will use the Z variable for convenience.

The general WKB solution can be written, to first order in \hbar , as

$$\Psi^E(Z) \sim (2E + Z^2)^{-1/4} \left(\alpha(\hbar) e^{+i\phi(Z_0, Z)/\hbar} + \beta(\hbar) e^{-i\phi(Z_0, Z)/\hbar} \right), \quad (25)$$

where the exponents are now the classical action integrals, taken from an (adjustable) origin Z_0 ,

$$\phi(Z_0, Z) = \int_{Z_0}^Z P_E(Z') dZ', \quad P_E(Z) \equiv \sqrt{2E + Z^2} \quad (26)$$

with the determination of the square root $P_E(Z)$ fixed by the cuts indicated on fig. 2 (left) and by $P_E(0) > 0$. This approximation is valid for $\hbar \rightarrow 0$, when Z stays far enough from the two turning points $Z_\pm = \pm i\sqrt{2E}$ in the sense that $|\phi(Z_\pm, Z)| \gg \hbar$. The coefficients α and β a priori depend upon \hbar and the region of the complex

plane where Z lies. More precisely, the complex Z -plane is to be partitioned by the Stokes lines, specified for each turning point by the condition

$$i\phi(Z_{\pm}, Z)/\hbar \quad \text{real.} \quad (27)$$

Three such lines emanate from every turning point. When the variable Z crosses a Stokes line, the coefficients α and β change according to connection rules (see [19] for instance); the application of these rules yields the global structure of the solution. For full consistency, no Stokes line should link two turning points; this restriction forces us to slightly rotate \hbar into the complex plane, as $\hbar \rightarrow e^{i\epsilon} \hbar$, with the resulting partition of the plane drawn on fig. 2 (left). The explicit form of exponentially small WKB contributions is generally sensitive to the choice $\epsilon = \pm 0$. However, such is not the case for the subsequent results at the order to which they will be expressed, so that we may ultimately reset $\epsilon = 0$.

Before studying a particular solution, we introduce the hyperbolic angle variable $\theta = \text{arcsinh}(Z/\sqrt{2E})$ which allows to integrate the action in closed form, as

$$\phi(Z_0, Z) = \frac{E}{2} [\sinh(2\theta') + 2\theta']_{\theta_0}^{\theta} = \frac{1}{2} \left[Z' \sqrt{2E + Z'^2} + \log(Z' + \sqrt{2E + Z'^2}) \right]_{Z_0}^Z; \quad (28)$$

the turning points correspond to $\theta_{\pm} = \pm i\pi/2$; the action values $\phi(0, Z_{\pm}) = \pm i\pi E/2$ are frequently needed.

We fully describe one eigenfunction as an example, $\Psi_+^E(Z)$ (corresponding to $\lambda = 0$). We identify its WKB form first in the regions \mathcal{S}' , \mathcal{S}_1 , \mathcal{S}_2 , by noticing that this eigenfunction must be exponentially decreasing for $Z \rightarrow \infty$ in a sector around $\arg Z = -3\pi/4$ (i.e., $z \rightarrow -\infty$) overlapping with those three regions, and then in the remaining regions by using the connection rules. The result is

$$\begin{aligned} \Psi_+^E(Z) &\sim \frac{C(\hbar)}{P_E(Z)^{1/2}} e^{+i\phi(0,Z)/\hbar} && \text{in the regions } \mathcal{S}', \mathcal{S}_1, \mathcal{S}_2 \\ \Psi_+^E(Z) &\sim \frac{C(\hbar)}{P_E(Z)^{1/2}} e^{-\pi E/2\hbar} \left(e^{+i\phi(Z_+,Z)/\hbar} + i e^{-i\phi(Z_+,Z)/\hbar} \right) && \text{in } \mathcal{S}_0 \\ \Psi_+^E(Z) &\sim \frac{C(\hbar)}{P_E(Z)^{1/2}} e^{+\pi E/2\hbar} \left(e^{+i\phi(Z_-,Z)/\hbar} - i e^{-i\phi(Z_-,Z)/\hbar} \right) && \text{in } \mathcal{S}_3. \end{aligned} \quad (29)$$

The overall normalization factor $C(\hbar)$ is determined by comparison with the direct saddle-point evaluation of the integral (14):

$$C(\hbar) = K(2\pi\hbar)^{1/4} e^{-\pi E/4\hbar} e^{-i\pi/8} (E/e)^{iE/2\hbar}. \quad (30)$$

Eqs. (29) readily yield the WKB expansions for the general solution as

$$\begin{aligned} \Psi_{\lambda}^E(Z) &\sim \frac{C(\hbar)}{P_E(Z)^{1/2}} \left[e^{+i\phi(0,Z)/\hbar} + \lambda e^{-i\phi(0,Z)/\hbar} \right] && \text{in } \mathcal{S}' \\ \Psi_{\lambda}^E(Z) &\sim \frac{C(\hbar)}{P_E(Z)^{1/2}} \left[e^{+i\phi(0,Z)/\hbar} + (\lambda - c_-) e^{-i\phi(0,Z)/\hbar} \right] && \text{in } \mathcal{S}_0 \end{aligned}$$

$$\begin{aligned}
\Psi_\lambda^E(Z) &\sim \frac{C(\hbar)}{P_E(Z)^{1/2}} \left[(1 - \lambda c_+) e^{+i\phi(0,Z)/\hbar} + \lambda e^{-i\phi(0,Z)/\hbar} \right] && \text{in } \mathcal{S}_1 \quad (31) \\
\Psi_\lambda^E(Z) &\sim \frac{C(\hbar)}{P_E(Z)^{1/2}} \left[(1 - \lambda c_-) e^{+i\phi(0,Z)/\hbar} + \lambda e^{-i\phi(0,Z)/\hbar} \right] && \text{in } \mathcal{S}_2 \\
\Psi_\lambda^E(Z) &\sim \frac{C(\hbar)}{P_E(Z)^{1/2}} \left[e^{+i\phi(0,Z)/\hbar} + (\lambda - c_+) e^{-i\phi(0,Z)/\hbar} \right] && \text{in } \mathcal{S}_3,
\end{aligned}$$

with the notations

$$c_\pm = -e^{\pm i\pi\nu} = \pm i e^{\pm \pi E/\hbar} \quad (c_- = 1/c_+). \quad (32)$$

5 Large values of the Husimi density

5.1 In the WKB framework

We study the particular solution $\Psi_+^E(Z)$ for a fixed positive energy E as an example. From the WKB expansions (29), we derive the Husimi density of this solution, using the hyperbolic angle as variable. In the regions \mathcal{S}' , \mathcal{S}_1 , \mathcal{S}_2 , away from the turning points, we obtain

$$\mathcal{H}_+^E(Z, \overline{Z}) \approx \frac{|C(\hbar)|^2}{[E(\cosh 2\Re(\theta) + \cos 2\Im(\theta))]^{1/2}} \exp \left\{ \frac{E}{\hbar} \left(-\cosh 2\Re(\theta) [\sin 2\Im(\theta) + 1] + \cos 2\Im(\theta) - 2\Im(\theta) \right) \right\}. \quad (33)$$

This formula shows that the Husimi measure concentrates semi-classically along the maxima of the exponential factor. Since the variable θ is restricted to the strip $|\Im(\theta)| < \pi/2$, those maxima occur on the line $\Im(\theta) = -\pi/4$, which corresponds exactly to the branch of hyperbola of energy E in the half-plane $\Im(Z) < 0$. In the region $\mathcal{S}_0 \cap \{\Im(Z) \leq 0\}$, $\mathcal{H}_+^E(Z, \overline{Z})$ also obeys eq. (33) up to exponentially small terms, so that the discussion concerns the whole E -hyperbola branch in the lower Z -half-plane. The above expression simplifies around this maximum curve, according to the following remarks. First of all, the variables (Z, \overline{Z}) are (up to a factor $-i$) symplectic transforms of the original variables (q, p) , so the expression of the classical energy $E = -\frac{1}{2}\overline{Z}^2 + V(Z)$, where $V(Z)$ is analytic, implies the following classical velocity along the E -energy curve :

$$\dot{Z} = i \frac{\partial E}{\partial \overline{Z}} = -i\overline{Z} \quad (34)$$

and along this curve, we also have $|Z|^2 = E \cosh 2\Re(\theta)$. Furthermore, if we decompose a small variation $\delta\theta$ as

$$\begin{aligned}
\delta Z_\parallel &= \sqrt{2E} \cosh \theta \Re(\delta\theta) \\
\delta Z_\perp &= i\sqrt{2E} \cosh \theta \Im(\delta\theta)
\end{aligned} \quad (35)$$

(δZ_\perp is a variation of Z perpendicularly to the E -hyperbola), then we obtain the following expression of the Husimi density around this maximum curve:

$$\mathcal{H}_+^E(Z, \overline{Z}) \approx |K|^2 \sqrt{2\pi\hbar} \frac{1}{|\dot{Z}|} e^{-2|\delta Z_\perp|^2/\hbar}; \quad (36)$$

that is, the density decreases as a Gaussian of constant width normally to the maximum curve, its height being given by the inverse of the phase-space velocity. This corresponds semi-classically to a conserved probability flux along this curve, and confirms earlier predictions [10] (cf. fig. 1, top left and bottom right).

As a new feature, by contrast, in the upper Z -half-plane there is a maximum curve in the region \mathcal{S}_0 only, and well below the anti-Stokes line where the zeros of $\Psi_+^E(Z)$ lie. This maximum curve is given by $\Im(\theta) = +\pi/4$, i.e., it is the other branch of the E -hyperbola. Around it, the Husimi density behaviour is precisely eq. (36) times the constant factor $\exp(-2\pi E/\hbar)$, an exponentially small contribution compared to that from the lower half-plane; hence this enhancement is semi-classically “invisible” but can be guessed on the log-plot in fig. 1, top right. (The correspondence between the z and Z variables is recalled on Fig. 2, right.)

5.2 Energies close to zero

Now using the expansions (24), we can analyze the large values of the Husimi density in the case where E/\hbar stays bounded, still in the semi-classical limit $\hbar \rightarrow 0$. If we still consider the function $\psi_+^E(z)$, we find a concentration along an invariant subset of the separatrix, i.e., the positive real and the imaginary z -axes. More precisely, if $|z|^2 \gg \hbar$, we have

$$\begin{aligned} \mathcal{H}_+^E(z, \bar{z}) &\sim |K|^2 \sqrt{2\pi\hbar} \frac{1}{|\dot{z}|} e^{-2E \arg(z)/\hbar} e^{-2\Im(z)^2/\hbar} \quad \text{when } |\arg(z)| < \frac{\pi}{4} \\ \mathcal{H}_+^E(z, \bar{z}) &\sim \frac{|K|^2}{\cosh(\pi E/\hbar)} \sqrt{\frac{\pi\hbar}{2}} \frac{1}{|\dot{z}|} e^{2E \arg(-z)/\hbar} e^{-2\Re(z)^2/\hbar} \quad \text{when } |\arg(-z)| < \frac{3\pi}{4}. \end{aligned} \quad (37)$$

We notice that both the longitudinal dependence of the density, and its Gaussian decrease away from the separatrix, are exactly the same as for a regular energy curve. Thus, away from the unstable fixed point $z = 0$, the singular limit $E \rightarrow 0$ behaves straightforwardly. Here, however, the Husimi density is also described exactly all the way down to the saddle-point (for $z \approx 0$ when $E \approx 0$), by the explicit formulae (21), e.g.,

$$\mathcal{H}_+^E(0, 0) = \frac{|K|^2}{\sqrt{8\pi}} \left| \Gamma\left(\frac{1}{4} + i\frac{E}{2\hbar}\right) \right|^2. \quad (38)$$

We can likewise obtain the rough shape of the Husimi density for a general solution ψ_λ^E . As before, whatever type of expansion we use, we find along each of the four half-axes (which are asymptotes to the classical energy curves)

$$\mathcal{H}_\lambda^E(z, \bar{z}) \approx I \frac{1}{|\dot{z}|} e^{-2|\delta Z_\perp|^2/\hbar} \quad (39)$$

where the constant I , depending on λ and on the half-axis we consider, can be interpreted semi-classically as the invariant intensity of a flux of particles moving with velocity $\dot{z} = \bar{z}$ along this branch of classical curve. For $E \gg 0$, the flux

is separately conserved along each of the two hyperbola branches: with obvious notations,

$$\begin{aligned} I_+ &= I_{-i} = |K|^2 \sqrt{2\pi\hbar} \\ I_- &= I_{+i} = |K|^2 |\lambda|^2 \sqrt{2\pi\hbar}. \end{aligned} \quad (40)$$

When the energy approaches its critical value 0, the intensities become

$$\begin{aligned} I_+ &= |K|^2 \sqrt{2\pi\hbar} \\ I_- &= |K|^2 \sqrt{2\pi\hbar} |\lambda|^2 \\ I_{+i} &= \frac{|K|^2 \sqrt{2\pi\hbar}}{2 \cosh(\pi E/\hbar)} \left\{ |\lambda|^2 e^{\pi E/\hbar} + 2\Im(\lambda) + e^{-\pi E/\hbar} \right\} \\ I_{-i} &= \frac{|K|^2 \sqrt{2\pi\hbar}}{2 \cosh(\pi E/\hbar)} \left\{ |\lambda|^2 e^{-\pi E/\hbar} - 2\Im(\lambda) + e^{\pi E/\hbar} \right\}. \end{aligned} \quad (41)$$

Now the flux is only conserved globally: it is easy to check that $I_{+i} + I_{-i} = I_+ + I_-$.

6 Asymptotic study of the zeros

The asymptotic geometry of the zeros for a general solution can be deduced from the following general principles. When a function $f(Z)$ has an asymptotic expansion (within a sector) combining two exponential behaviours, the function can only vanish when both exponential factors are of the same order of magnitude. Thus, the two exponents must have equal real parts: this necessary condition defines the anti-Stokes lines of the problem in the complex Z -plane. Zeros of the function can then only develop along anti-Stokes lines (always in the large- $|Z|$ approximation), and provided both exponentials are present in the given sectorial expansion, with fixed non-zero prefactors.

6.1 Energies close to zero - general case

Here the expansions (24) have to be used, and it is simpler to work in the rotated Z variable. Then the exponential factors read as $e^{+iZ^2/2\hbar}$ and $e^{-iZ^2/2\hbar}$, and the anti-Stokes lines on which they balance each other, namely the bisecting lines L_j of the quadrants S_j , are simply the real and imaginary Z -axes (fig. 2, right). Now, for each fixed j , two independent solutions $\Phi_{\pm}^{(j)}$ of eq. (17) can be specified by imposing single-exponential asymptotic behaviours along L_j , as $\Phi_{\pm}^{(j)} \sim f_{\pm}^{(j)}(Z) e^{\pm iZ^2/2\hbar}$. A general solution $\Psi(Z)$ is then proportional to $[\Lambda \Phi_+^{(j)} + \Phi_-^{(j)}]$ for some $\Lambda \in \overline{\mathbb{C}}$, and satisfies

$$\Psi(Z) \propto \Lambda f_+^{(j)}(Z) e^{+iZ^2/2\hbar} + f_-^{(j)}(Z) e^{-iZ^2/2\hbar}, \quad Z \rightarrow \infty \text{ in } S_j, \quad (42)$$

whence the condition $\Psi(Z) = 0$ in the sector S_j asymptotically reads as

$$Z^2/\hbar \sim (-1)^j 2\pi m + i \log \left[\Lambda r^{(j)}(Z) \right], \quad \text{for } m \rightarrow +\infty, \quad r^{(j)}(Z) \equiv -f_+^{(j)}(Z)/f_-^{(j)}(Z). \quad (43)$$

This yields an asymptotic sequence of zeros, as: $Z_m^{(j)} \sim e^{ij\pi/2} \sqrt{2\pi m\hbar}$ to leading order; thereupon, to the order $O(1)$ included,

$$Z_m^{(j)2}/\hbar \sim (-1)^j 2\pi m + i \log r^{(j)}(e^{ij\pi/2} \sqrt{2\pi m\hbar}) + i \log \Lambda + O(m^{-1} \log m), \quad m \rightarrow +\infty. \quad (44)$$

The final square-root extraction is straightforward,

$$Z_m^{(j)}/\sqrt{\hbar} \sim e^{ij\pi/2} \left(\sqrt{2\pi m} + (-1)^j i \frac{\log r^{(j)}(e^{ij\pi/2} \sqrt{2\pi m\hbar}) + \log \Lambda}{2\sqrt{2\pi m}} + O\left(\frac{\log^2 m}{m^{3/2}}\right) \right) \quad (45)$$

so that the simpler form (44) will be preferred for further displays of results.

When the asymptotic analysis concerns a fixed linear combination given as $[\lambda D_\nu(y) + D_\nu(-y)]$, Λ turns into a sector-dependent function $\Lambda^{(j)}(\lambda)$, which is the linear fractional transformation induced by the change of basis $\{D_\nu(y), D_\nu(-y)\} \rightarrow \{\Phi_+^{(j)}(Z), \Phi_-^{(j)}(Z)\}$. The equations for zeros like (44) become singular for the two values of λ which map to $\Lambda^{(j)} = 0$ or ∞ , simply because they yield the pure $\Phi_-^{(j)}$ or $\Phi_+^{(j)}$ solutions which have no zeros (at least asymptotically) in this sector S_j .

We now list more explicit results. In the sector S_0 , corresponding to $\{0 < \arg y < +\pi/2\}$,

$$\lambda D_\nu(y) + D_\nu(e^{-i\pi} y) \sim (\lambda + e^{-i\pi\nu}) y^\nu e^{-y^2/4} + \frac{\sqrt{2\pi}}{\Gamma(-\nu)} y^{-\nu-1} e^{+y^2/4}. \quad (46)$$

Upon the substitutions $\Lambda^{(0)}(\lambda) r^{(0)}(Z) \equiv (\sqrt{2\pi}/\Gamma(-\nu)) y^{-2\nu-1}/(\lambda + e^{-i\pi\nu})$, $y = \sqrt{2/\hbar} e^{i\pi/4} Z$ and $\nu = -\frac{1}{2} - \frac{iE}{\hbar}$, the asymptotic equation (44) for zeros becomes

$$\frac{Z_m^{(0)2}}{\hbar} \sim (2m-1)\pi - \frac{E}{\hbar} \log 4m\pi i - i \log \frac{\Gamma(\frac{1}{2} + i\frac{E}{\hbar})}{\sqrt{2\pi}} - i \log(\lambda + i e^{-\pi E/\hbar}), \quad -\frac{\pi}{4} < \arg Z < +\frac{\pi}{4}. \quad (47)$$

A geometrical interpretation will prove useful. Let C_\pm be the two circles in the λ -plane respectively specified by the parameters (cf. eq. (32) and fig. 3)

$$\text{centers: } c_\pm = \pm i e^{\pm\pi E/\hbar}, \quad \text{radii: } R_\pm = (1 + e^{\pm 2\pi E/\hbar})^{1/2} \quad (48)$$

(they are both centered on the imaginary axis and intersect orthogonally at $\lambda = +1$ and -1). Let us also write, for real t , $\Gamma(\frac{1}{2} + it)/\sqrt{2\pi}$ in polar form as $(2 \cosh \pi t)^{-1/2} e^{i\Theta(t)}$, defining the phase $\Theta(t)$ by continuity from $\Theta(0) = 0$. The formula (47), and its partners in the other sectors, then become:

in $S_0 = \{-\pi/4 < \arg Z < +\pi/4\}$,

$$\frac{Z_m^{(0)2}}{\hbar} \sim (2m-1)\pi - \frac{E}{\hbar} \log 4m\pi + \Theta(E/\hbar) - i \log \frac{\lambda - c_-}{R_-} \quad (\lambda \notin \{c_-, \infty\}) \quad (49)$$

in $S_1 = \{+\pi/4 < \arg Z < +3\pi/4\}$,

$$-\frac{Z_m^{(1)2}}{\hbar} \sim (2m-1)\pi + \frac{E}{\hbar} \log 4m\pi - \Theta(E/\hbar) + i \log \frac{\lambda^{-1} - c_+}{R_+} \quad (\lambda \notin \{0, c_+\}) \quad (50)$$

in $S_2 = \{-5\pi/4 < \arg Z < -3\pi/4\}$,

$$\frac{Z_m^{(2)2}}{\hbar} \sim (2m-1)\pi - \frac{E}{\hbar} \log 4m\pi + \Theta(E/\hbar) - i \log \frac{\lambda^{-1} - c_-}{R_-} \quad (\lambda \notin \{0, c_+\}) \quad (51)$$

in $S_3 = \{-3\pi/4 < \arg Z < -\pi/4\}$,

$$-\frac{Z_m^{(3)2}}{\hbar} \sim (2m-1)\pi + \frac{E}{\hbar} \log 4m\pi - \Theta(E/\hbar) + i \log \frac{\lambda - c_+}{R_+} \quad (\lambda \notin \{c_+, \infty\}). \quad (52)$$

For general values of the parameters we cannot get more precise information this way, except by going to higher orders (but still in the asymptotic sense). We have yet no idea about the position, or even existence, of small zeros. Our subsequent strategy will be to start from very special cases for which the pattern of zeros is well known, and from there to vary continuously the parameters E and λ and keep track of the zeros along these deformations: zeros are topological defects, so they move continuously w.r. to both parameters. We will then exploit symmetries of eq. (17), especially the reality of its solutions (a real function of a complex variable t is one satisfying $f(\bar{t}) = \overline{f(t)}$). Eq. (17) is a differential equation with real coefficients, hence it admits real solutions, whose zeros are symmetrical w. r. to the real Z -axis. During a deformation of a real solution, zeros could then only leave (or enter) the real axis in conjugate pairs, but at the same time the functions considered here (solutions of a second-order equation) cannot develop double zeros; consequently, each zero is bound to stay permanently real (or nonreal) in the course of a real deformation.

6.2 Even-odd solutions of zero energy

We use the $E = 0$ expressions eq. (20) in terms of the Bessel functions $J_{\pm 1/4}(Z^2/2\hbar)$ to view the pattern of zeros more precisely in this particular case.

We know that, for real μ , $t^{-\mu} J_\mu(t)$ is a real even function having only real zeros $\pm j_{\mu,m}$, $m = 1, 2, \dots$, with $j_{\mu,m} > 0$ and $j_{\mu,m} \sim \pi(m + \frac{\mu}{2} - \frac{1}{4})$ for large m . This translates into the Z variable as follows.

For $\lambda = +1$: the even solution (fig. 1, middle right)

$$\Psi_{+1}^0(Z) = K \left(2\pi^3/\hbar\right)^{1/4} Z^{1/2} J_{-1/4}\left(\frac{Z^2}{2\hbar}\right) \quad (53)$$

(a real function for K real), is not just even but also invariant under $Z \rightarrow iZ$; all its zeros are purely real or imaginary, the m -th positive zero admits the approximation

$$Z_m^{(0)}|_{\lambda=+1} \sim \sqrt{\hbar(2m\pi - 3\pi/4)}, \quad (54)$$

and all other zeros follow by the rotational symmetry of order 4.

For $\lambda = -1$: the odd solution (fig. 1, bottom left)

$$\Psi_{-1}^0(Z) = K e^{i\pi/4} \left(2\pi^3/\hbar\right)^{1/4} Z^{1/2} J_{1/4}\left(\frac{Z^2}{2\hbar}\right) \quad (55)$$

has exactly the same symmetries for its zeros as the even one (because the auxiliary function $e^{-i\pi/4} \Psi_{-1}^0(Z)/Z$ has all the symmetries of $\Psi_{+1}^0(Z)$); besides an obvious zero at the origin, the m -th positive zero of $\Psi_{-1}^0(Z)$ lies approximately at

$$Z_m^{(0)}|_{\lambda=-1} \sim \sqrt{\hbar(2m\pi - \pi/4)}. \quad (56)$$

6.3 Even–odd solutions of non-zero energy

If we “switch on” the energy, keeping $\lambda = +1$, the solutions will not be Bessel functions any longer, but they still exhibit interesting features. Equation (17) has real coefficients, hence its even and odd solutions are real up to a constant factor, i.e., up to an adjustment of $\arg K$. For the even solution $\Psi_{+1}^E(Z)$, the reality condition is

$$\Psi_{+1}^E(0) = K \left(\frac{2}{\pi} \right)^{1/4} (2\hbar)^{\frac{iE}{2\hbar}} \Gamma \left(\frac{1}{4} + \frac{iE}{2\hbar} \right) \quad \text{real}. \quad (57)$$

This even solution can be seen as a real deformation of the solution (53). It maintains the symmetry w.r. to the origin and to the two Z coordinate axes; only the $\pi/2$ rotation symmetry is lost for $E \neq 0$. Due to the two mirror symmetries, as explained above, the only possible motion of the zeros during this deformation is a “creeping without crossing” along the four half-axes, symmetrically w.r. to the origin. This can be checked on the $O(1)$ terms of the expansions (49–52), and on the sequence of plots: fig. 1 (middle right), fig. 6 (right), fig. 1 (bottom right). At the same time, this deformation allows to properly count the zeros at all energies, by continuity from $E = 0$ where eq. (54) does count the zeros: in each of the expansions (49–52), $Z_m^{(j)}$ remains the actual m -th zero on the half-axis L_j if the corresponding complex log functions are defined at $\lambda = +1$ as

$$\log(1-c_+) = \log|1-c_+| - i \arctan e^{+\pi E/\hbar}, \quad \log(1-c_-) = \log|1-c_-| + i \arctan e^{-\pi E/\hbar} \quad (58)$$

where the arctan function has the usual range $(-\pi/2, \pi/2)$.

The same analysis can be performed for the odd real solution $\Psi_{-1}^E(Z)$ of (17), a deformation of the solution (55), for which the reality condition is

$$\frac{d\Psi_{-1}^E}{dZ}(0) = K \left(\frac{2^7}{\pi} \right)^{1/4} (2\hbar)^{-\frac{1}{2} + \frac{iE}{2\hbar}} \Gamma \left(\frac{3}{4} + \frac{iE}{2\hbar} \right) e^{i\pi/4} \quad \text{real}. \quad (59)$$

6.4 Real solutions

We now consider more general families of real solutions, i.e., $\Psi_\lambda^E(\bar{Z}) = \overline{\Psi_\lambda^E(Z)}$, $\forall Z \in \mathbb{C}$. These exist only for certain values of λ , for which we have to adjust K . Since (17) is a second-order equation with real coefficients, it has the real solutions

$$\Psi^E(Z) = \kappa \left(\Psi_{+1}^E(Z) + t \Psi_{-1}^E(Z) \right), \quad \text{for } \kappa \in \mathbb{R}^*, \quad t \in \mathbb{R} \cup \{\infty\} = \overline{\mathbb{R}}. \quad (60)$$

Under the change of basis $\{\Psi_{+1}^E(Z), \Psi_{-1}^E(Z)\} \longrightarrow \{D_\nu(y), D_\nu(-y)\}$, the set $\{t \in \overline{\mathbb{R}}\}$ is mapped to a circle in the projective λ -plane, passing through $\lambda|_{t=0} = +1$, $\lambda|_{t=\infty} =$

–1. The full circle can be determined long-hand using eqs. (57–59), but more easily by asking the expansions (49), (51) to yield asymptotically real zeros as reality demands: the resulting λ -circle is C_- (note that $\lambda \in C_- \iff 1/\lambda \in C_-$).

Let us now analyze the motion of the zeros in the four sectors as we vary λ around C_- anti-clockwise from 1 to $e^{2i\pi}$. We already know that the real zeros cannot leave the real axis by symmetry. In the expansions (49) and (51) for S_0 and S_2 respectively, the only modifications are that $\arg(\lambda - c_-)$ increases by 2π , and $\arg(\lambda^{-1} - c_-)$ decreases by 2π , inducing a re-labeling of the large zeros in those two sectors. Hence each large positive or negative zero creeps to the right until it reaches the former position of its right neighbour after one cycle. The small zeros, trapped on a real bounded interval in-between by reality, and unable to cross one another, can then only follow the same homotopic pattern of behaviour.

In each of the two remaining sectors, by contrast, the zeros are not confined to the imaginary axis whereas the cycle C_- is homotopically trivial in the Riemann surface of the relevant logarithmic function. According to the expansions in S_1 (resp. S_3), the large zeros in these sectors perform a clockwise (resp. anti-clockwise) cycle beginning and ending at their location on the imaginary axis for $\lambda = 1$. The geometric relation $\overline{\lambda - c_+} = R_+^2(\lambda^{-1} - c_+)^{-1}$ is the asymptotic remnant of reality: $\{\Psi(Z) = 0 \Rightarrow \Psi(\overline{Z}) = 0\}$. This motion in S_1 and S_3 has been thus shown only for large zeros, but we may argue a similar behaviour for the smaller ones by homotopy; moreover, by reality these zeros cannot cross the real axis and are confined to a bounded region around the origin (contrary to the real zeros, they cannot migrate to infinity when λ keeps revolving around C_-); orbits of non-real zeros during the described λ -cycle are also symmetrical w.r. to the imaginary axis, thanks to a $\lambda \leftrightarrow 1/\lambda$ symmetry of the real solutions.

The evolution of all the zeros under the λ -cycle C_- is globally depicted for $E = 0$ on fig. 4 (left).

Similarly, the solutions corresponding to $\lambda \in C_+$ can be chosen real w.r. to the variable iZ (observing that eq. (17) is invariant under the change $\{Z \rightarrow iZ, E \rightarrow -E\}$), and analyzed likewise.

6.5 Singular values of λ

Each of the expansions (49–52) becomes singular for two values of λ from the set $\{0, \infty, c_-, c_+\}$. The solutions are then $\psi_{\pm}^E(z), \psi_{\pm}^{-E}(iz)$, corresponding to “pure D_{ν} functions”, and eqs. (24) clearly show that $D_{\nu}(y)$ has large zeros only in two out of four sectors, namely along the pair of adjacent anti-Stokes lines $\{\arg y = \pm 3\pi/4\}$. That is why the zeros in the two other sectors must “escape to infinity” as λ moves towards one of its special values. Let for instance λ decrease from +1 (the even solution case) to the special value 0 along the interval $[0, 1]$. For simplicity we first restrict ourselves to the case $E = 0$, where the eigenfunctions are combinations of Bessel functions. The zeros’ expansions (49–52) (with $R_{\pm}|_{E=0} = \sqrt{2}$) then become singular in the sectors S_1 and S_2 , whereas they stay perfectly uniform in the two other sectors. In S_2 , eq. (51) holds uniformly as $Z_m^{(2)2}/\hbar \rightarrow \infty$, which amounts

to $-\log \lambda + 2\pi m \gg 1$, and the same conclusion is reached for eq. (50) in S_1 . As $\lambda \rightarrow +0$, the two formulae merge into a single one,

$$Z_n^2/\hbar \sim i \log \frac{\lambda}{\sqrt{2}} + (2n-1)\pi \quad \text{in } S_1 \cup S_2 \quad \text{for any } n \in \mathbb{Z} \quad (61)$$

where the global counting index $n \in \mathbb{Z}$ matches with m in the sector S_2 for $n \gg 0$ and with $(-m+1)$ in S_1 for $n \ll 0$. These zeros thus tend to follow the hyperbola branch $\{2\Re(Z)\Im(Z) = \hbar \log \lambda/\sqrt{2}, \Re(Z) < 0\}$, which itself recedes to infinity as $\lambda \rightarrow +0$, as can be seen on fig. 4 (right) followed by fig. 1 (middle left).

This description can be generalized to the case of a non-vanishing (but small) energy. The asymptotic condition for zeros in $S_1 \cup S_2$ when $\lambda \rightarrow 0$ must now be drawn from eq. (43) itself and reads as

$$\frac{Z_n^2}{\hbar} \approx (2n-1)\pi - i \log \left(\frac{\lambda^{-1} - c_{\mp}}{R_{-}} \right) - \frac{E}{\hbar} \log \left(2 \frac{Z_n^2}{\hbar} \right) + \Theta(E/\hbar) \quad \text{for } n \rightarrow \pm\infty. \quad (62)$$

For small values of λ , these zeros tend to follow asymptotically two half-branches of hyperbolae which differ as $n \rightarrow +\infty$ or $-\infty$ (because of the $\Im(\log Z_n^2)$ contribution); the matching between this set of zeros for small λ and the set of zeros of Ψ_{+1}^E on $\mathbb{R}_{-} \cup i\mathbb{R}_{+}$ can be done as in the case $E = 0$.

6.6 WKB expansions of zeros at a fixed non-vanishing energy

We first consider the particular solution $\Psi_{+}^E(Z)$. In the semi-classical limit of eqs. (29), $\Psi_{+}^E(Z)$ can vanish only within the regions \mathcal{S}_0 and \mathcal{S}_3 and along anti-Stokes lines, now defined by the conditions: $\phi(Z_{\pm}, Z)/\hbar$ real, respectively. From the complete set of anti-Stokes lines (shown on fig. 5 top left, with $\arg \hbar = 0$ henceforth), the presently relevant ones are: in \mathcal{S}_3 , the imaginary half-axis below Z_{-} ; and in \mathcal{S}_0 , the anti-Stokes line from Z_{+} asymptotic to the positive real axis (fig. 5, bottom right). The zeros themselves are given asymptotically by the equations

$$\begin{aligned} \phi(Z_{+}, Z) &= (+m - 1/4)\hbar\pi, & m \in \mathbb{N}, m \gg 1 & \quad \text{in } \mathcal{S}_0 \\ \phi(Z_{-}, Z) &= (-m + 1/4)\hbar\pi, & m \in \mathbb{N}, m \gg 1 & \quad \text{in } \mathcal{S}_3. \end{aligned} \quad (63)$$

Finally, the expansions

$$\phi(Z_{+}, Z) \sim +Z^2/2 \quad \text{when } Z \rightarrow +\infty, \quad \phi(Z_{-}, Z) \sim +Z^2/2 \quad \text{when } Z \rightarrow -i\infty \quad (64)$$

restore the former large zero behaviours, $Z_m^{(j)} \sim e^{ij\pi/2} \sqrt{2\hbar m\pi}$ for $j = 0, 3$ respectively.

We can also see how the zeros in regions \mathcal{S}_1 and \mathcal{S}_2 go to infinity for a more general eigenfunction $\Psi_{\lambda}^E(Z)$, when the parameter λ decreases from 1 to 0 along

$[0, 1]$ as in subsection (6.5), but now for a fixed non-vanishing energy. We will then be able to compare the results in the two frameworks.

Using the WKB expansions (31) in the different regions of the Z -plane, we study the equation $\Psi_\lambda^E(Z) = 0$ in each of them [20]. For $\lambda = 0$ we found zeros along only two anti-Stokes lines. For a general value, there will be zeros in all regions (and, inasmuch as λ varies independently of \hbar , those zeros are not confined near the above anti-Stokes lines). Moreover, we know from symmetry properties that for $\lambda = \pm 1$, the zeros can only lie on the real and imaginary axes. It is also obvious, from the different expansions, that the zeros' pattern depends on the ratio $\lambda/c_- = \lambda c_+$ (cf. eq. (32)).

In the range $1 > \lambda \gg |c_-|$, the differences between the formulae (31) for regions \mathcal{S}' , \mathcal{S}_0 , \mathcal{S}_2 are irrelevant as far as the position of the zeros is concerned, so that the first one suffices to localize the zeros in those three regions by means of the equations

$$\begin{aligned}\Im \phi(0, Z) &= -(i\hbar/2) \log \lambda \\ \Re \phi(0, Z) &= \hbar\pi/2 \mod \hbar\pi.\end{aligned}\tag{65}$$

For $\lambda = 1$, the zeros are exactly real by symmetry. When λ decreases towards $|c_-|$, the curve (65) gets deformed towards Z_+ , keeping the real axis as asymptote at both ends. At the same time, the zeros in $\mathcal{S}_1 \cup \mathcal{S}_3$ stay along the imaginary axis. When $\lambda \approx |c_-|$, there are zeros along all anti-Stokes lines from Z_+ and along the imaginary axis in \mathcal{S}_3 . When $\lambda \ll |c_-|$, the zeros along the anti-Stokes lines in $\mathcal{S}_0 \cup \mathcal{S}_3$ stabilize, whereas the ones in the regions $\mathcal{S}_1 \cup \mathcal{S}_2$ lie along the curve (65), which recedes to infinity when $\lambda \rightarrow 0$ as in the previous subsection, keeping $i\mathbb{R}_+$ and \mathbb{R}_- as asymptotes. All these phenomena appear on the sequence of plots in fig. 5. Once more, we can recover the previous asymptotic large zeros by expanding the action integrals $\phi(0, Z)$ along the four half-axes.

7 Conclusion

The above study should help to better understand more complicated 1-d systems when the eigenenergy is very near a saddle-point value and standard WKB theory fails.

This can be illustrated upon the eigenstates of a quantum Harper model. The classical Harper Hamiltonian is $H_H = -\cos(2\pi P) - \cos(2\pi Q)$ on the torus phase space ($Q \mod 1, P \mod 1$). We have quantized it on the Hilbert space of wavefunctions with periodic boundary conditions, which has a finite dimension N to be identified with $(2\pi\hbar)^{-1}$, and taken $N = 31$ for calculations. We have then selected the eigenfunction Ψ_n immediately below the separatrix energy $E = 0$; it is an even state having the quantum number $n = 14$, and its Husimi density over the torus is plotted on fig. 6, left (cf. also [14] 1990, fig. 2a). Now, by expanding the Hamiltonian near one saddle-point like ($Q = 0, P = -1/2$) we recover a quadratic-barrier problem. This suggests to compare Ψ_{14} with the even dilator eigenfunction $\Psi_{+1}^E(Z)$

for $E/\hbar \equiv 2\pi N|E_{14}|/(2\pi)^2$ and $z \equiv \hbar^{-1/2} e^{i\pi/4}(Q - iP)/\sqrt{2} \approx e^{i\pi/4} 10.(Q - iP)$ (see fig. 6 right). We then observe that not only the high densities of both figures around the saddle-points fit very nicely (a result to be expected from semiclassical comparison arguments [13, 10]), but also, more surprisingly, the sequences of zeros for the Harper eigenfunction match the comparison zeros as well, and not just near the saddle-points but practically all the way out to the extremal points; at these points the lines supporting the zeros intersect and the correspondence must fail, but this happens much beyond its reasonable range of validity anyway.

References

- [1] Y. Colin de Verdière and B. Parisse, *Equilibre instable en régime semi-classique I*, Comm. Partial Differential Equations **19**, 1535–1563 (1994); *II*, Ann. Inst. Henri Poincaré (Physique Théorique) **61**, 347–367 (1994)
- [2] P.M. Bleher, *Semiclassical quantization rules near separatrices*, Commun. Math. Phys. **165**, 621–640 (1994)
- [3] R. Brummelhuis, T. Paul and A. Uribe, *Spectral estimates around a critical level*, Duke Math. J. **78**, 477–530 (1995)
- [4] V. Bargmann, *On a Hilbert space of analytic functions and an associated integral transform*, Comm. Pure Appl. Math. **XIV**, 187–214 (1961) and **XX**, 1–101 (1967)
- [5] J.R. Klauder and B. Skagerstam, *Coherent States*, World Scientific, Singapore (1985)
- [6] A. M. Perelomov, *Generalized coherent states and their applications*, Springer, Berlin (1986)
- [7] W.-M. Zhang, D. H. Feng and R. Gilmore, *Coherent states: Theory and some applications*, Rev. Mod. Phys. **62**, 867–927 (1990)
- [8] R.P. Boas Jr., *Entire functions*, Academic Press, New York (1954)
- [9] K. Husimi, *Some formal properties of the density matrix*, Proc. Phys.-Math. Soc. Jpn **22**, 264–314 (1940)
- [10] K. Takahashi, *Wigner and Husimi function in quantum mechanics*, J. Phys. Soc. Jpn **55**, 762–779 (1986), and *Distribution functions in classical and quantum mechanics*, Prog. Theor. Phys. Suppl. **98**, 109–156 (1989)
- [11] J. Kurchan, P. Leboeuf and M. Saraceno, *Semiclassical approximations in the coherent-state representation*, Phys. Rev. **A 40**, 6800–6813 (1989)
- [12] A. Voros, *WKB method in the Bargmann representation*, Phys. Rev. **A 40**, 6814–6825 (1989)
- [13] K. Takahashi, *Husimi function around hyperbolic point*, J. Phys. Soc. Jpn **55**, 1783–1786 (1986)

- [14] P. Leboeuf and A. Voros, *Chaos-revealing multiplicative representation of quantum eigenstates*, J. Phys. **A 23**, 1765–1774 (1990); and *Quantum nodal points as fingerprints of classical chaos*, in: *Quantum chaos: Between order and disorder*, G. Casati and B.V. Chirikov eds., Cambridge University Press, Cambridge, UK, 507–533 (1995)
- [15] P. Leboeuf, *Phase space approach to quantum dynamics*, J. Phys. **A 24**, 4575–4586 (1991)
- [16] J.-M. Tualle and A. Voros, *Normal modes of billiards portrayed in the stellar (or nodal) representation*, Chaos, Solitons & Fractals **5**, 1085–1102 (1995)
- [17] A. Erdélyi (ed.), *Higher transcendental functions* (Bateman Manuscript Project), vol. II chap. 8, McGraw-Hill (1953)
- [18] N.L. Balazs and A. Voros, *Wigner’s function and tunneling*, Ann. Phys. (NY) **199**, 123–140 (1990)
- [19] F.W.J. Olver, *Asymptotics and special functions*, Academic Press, New York (1974)
- [20] F.W.J. Olver, *Uniform asymptotic expansions for Weber parabolic cylinder functions of large orders*, J. of Research NBS **63 B**, 131–169 (1959)

Figure captions

Fig. 1. Contour plots of the Husimi densities $\mathcal{H}_\lambda^E(z, \bar{z})$ ($\hbar = K = 1$) for selected eigenfunctions ψ_λ^E of the quantum dilator \hat{H} , using uniform level spacing 0.2 (linear plots), except for the top-right plot (drawn in a logarithmic scale using the uniform level ratio $1/e$ from the maximum downwards). The zeros of the Husimi densities, constituting the stellar representation, are shown as dots (except in top row). Maxima in the $E = 0$ plots: $\mathcal{H}_{+, \max}^{E=0} \approx 3.6963$ at $z \approx 0.5409$ (at middle left); $\mathcal{H}_{+1}^{E=0}$ (even state, at middle right) very steeply peaks at $z = 0$, with maximum value ≈ 10.488 ; $\mathcal{H}_{-1}^{E=0}$ (odd state, at bottom left) vanishes at $z = 0$ and reaches its maximum value ≈ 2.0054 at the four points $i^j z_0$, $z_0 \approx 1.162$.

Fig. 2. Stokes regions for the asymptotic $\hbar \rightarrow 0$ expansions of the eigenfunctions of \hat{H} . Left: fixed E regime (eqs. (29),(31)), with $\arg \hbar = \epsilon > 0$ (the Stokes lines for $\epsilon \rightarrow -\epsilon$ are the left-right transposed of these); Z_\pm are the two turning points; cuts for the function $P_E(Z)$ are conveniently placed over the two thicker Stokes lines. Right: fixed E/\hbar regime (eqs. (24),(49)–(52)); this picture is the scaling limit of the preceding one for $E \rightarrow 0$ when $\epsilon = 0$ (except for the place of cuts).

Fig. 3. The complex plane of the coefficient λ with the circles C_- corresponding to Z -real solutions and C_+ corresponding to iZ -real solutions; the finite special values $0, c_-, c_+$ are marked (the fourth one being $\lambda = \infty$).

Fig. 4. Left: positions of the zeros of $\psi_\lambda^{E=0}(z)$ for four values of λ in anticlockwise succession on the circle C_- : $\lambda_0 = +1$, $\lambda_1 = (\sqrt{2}-1)i$, $\lambda_2 = -1$, and $\lambda_3 = (-\sqrt{2}-1)i$. Right: same for the decreasing positive sequence $\lambda_n = 10^{-n}$, $n = 0, 3, 6$; fig. 1 (middle left) displays the limiting special value $\lambda = 0$.

Fig. 5. Top left: the anti-Stokes lines for the semiclassical expansions of the eigenfunctions of \hat{H} in the fixed E regime. Remaining five plots: positions of the zeros of $\psi_\lambda^{E=+1}(z)$, exceptionally with $\hbar = 0.2$, for a decreasing positive sequence of the type: $\lambda = +1$; $|c_-| \ll \lambda < 1$; $\lambda = |c_-| (= e^{-\pi E/\hbar})$; $0 < \lambda \ll |c_-|$; $\lambda = 0$. The thicker curves are the portions of the $H = E$ hyperbola where the Husimi measure concentrates semiclassically.

Fig. 6. Left: 15th eigenstate of the Harper model quantized in dimension $N = 1/(2\pi\hbar) = 31$ (with periodic boundary conditions); $\Psi_{14}(Z)$ has to have a double zero at $(0,0)$ to yield the correct count of 14 zeros within the $\{H_H < E\}$ region (and $(31 - 14)$ outside) [14]; this Husimi density contour plot exceptionally uses level spacing 0.089 to match the spacing-to-maximum ratio of the comparison plot (next). Right: the Husimi density \mathcal{H}_{+1}^E serving as comparison function, plotted as in fig. 1 (maximum value ≈ 6.752 , at the origin).

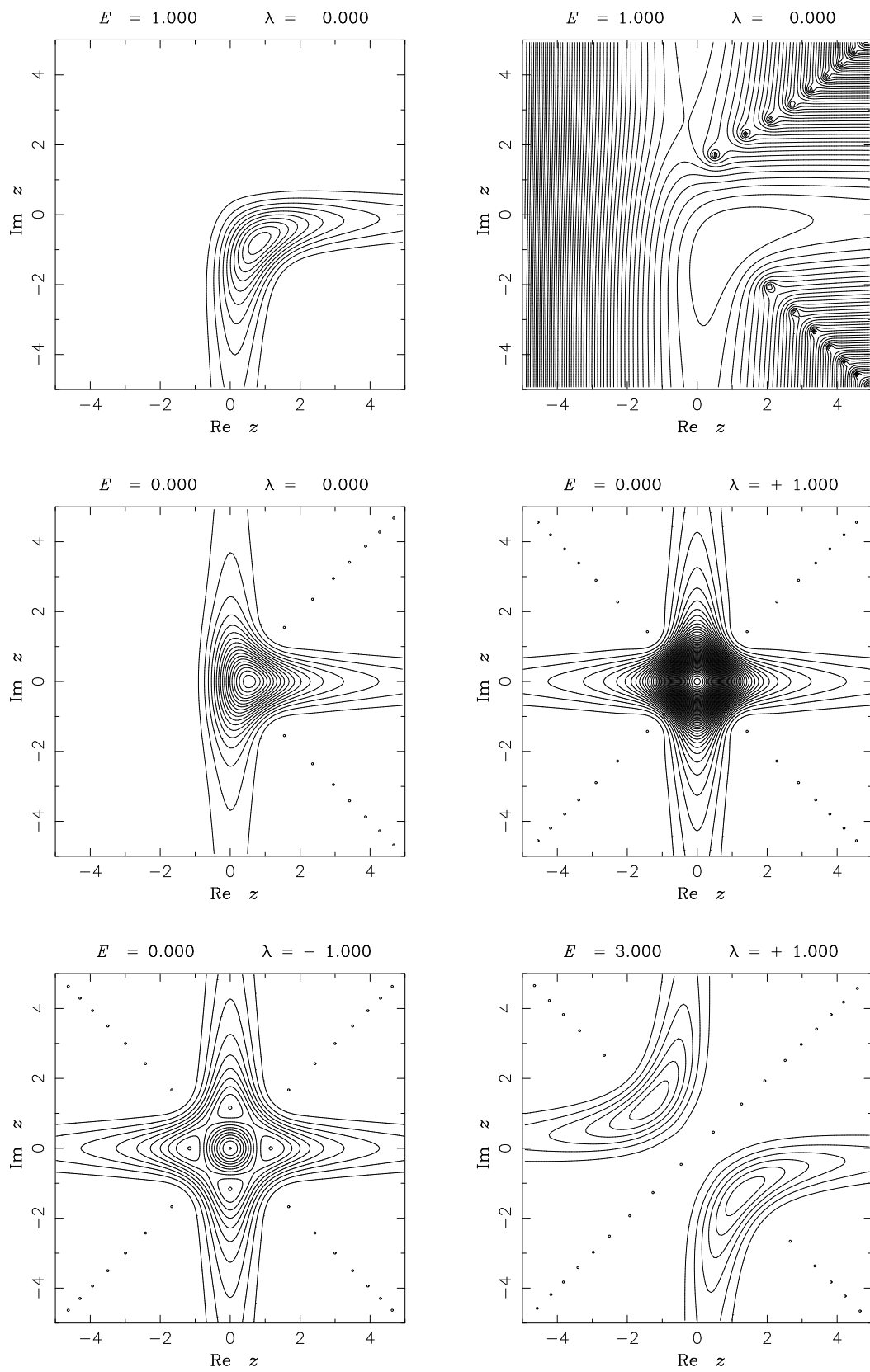


Figure 1:

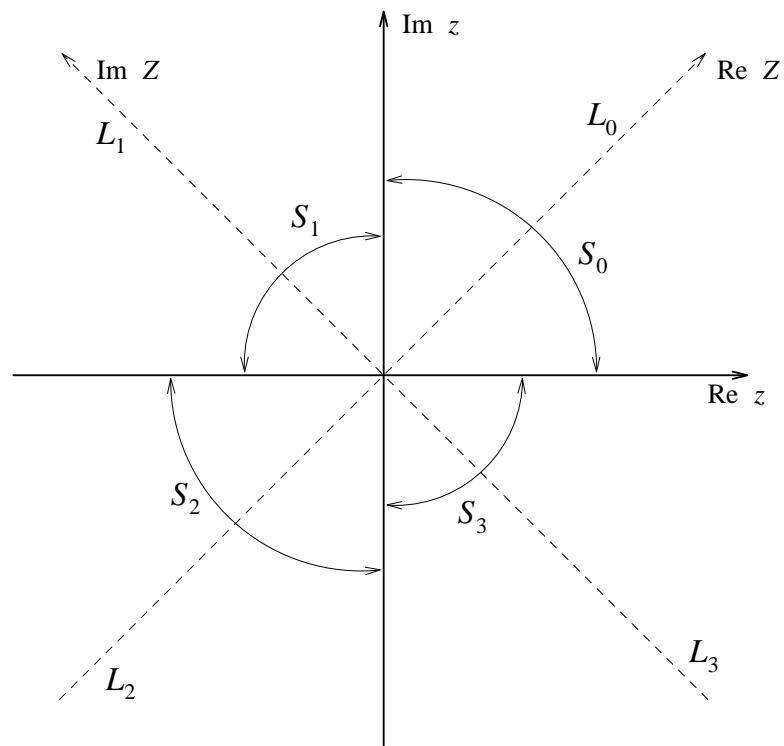
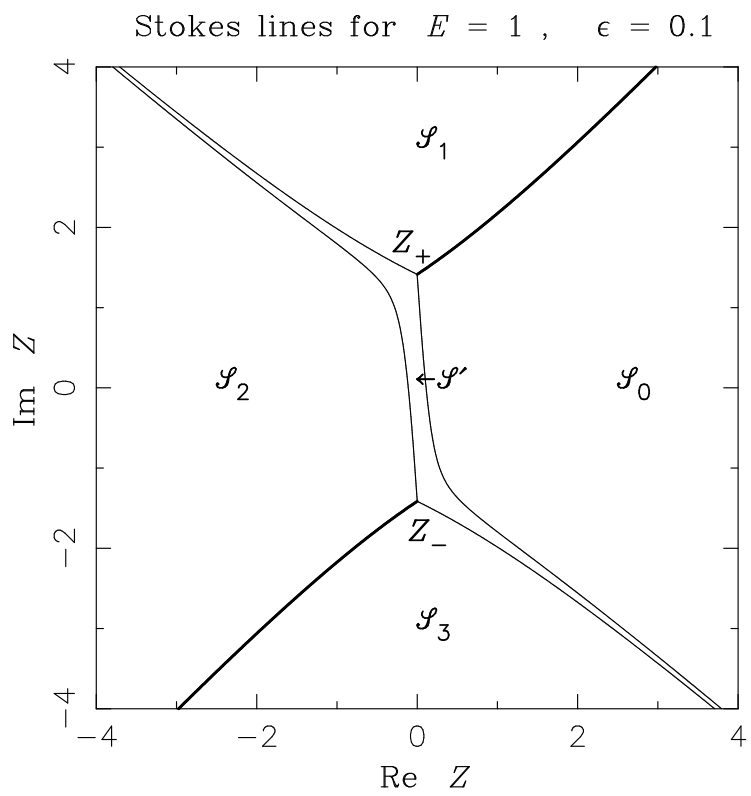


Figure 2:

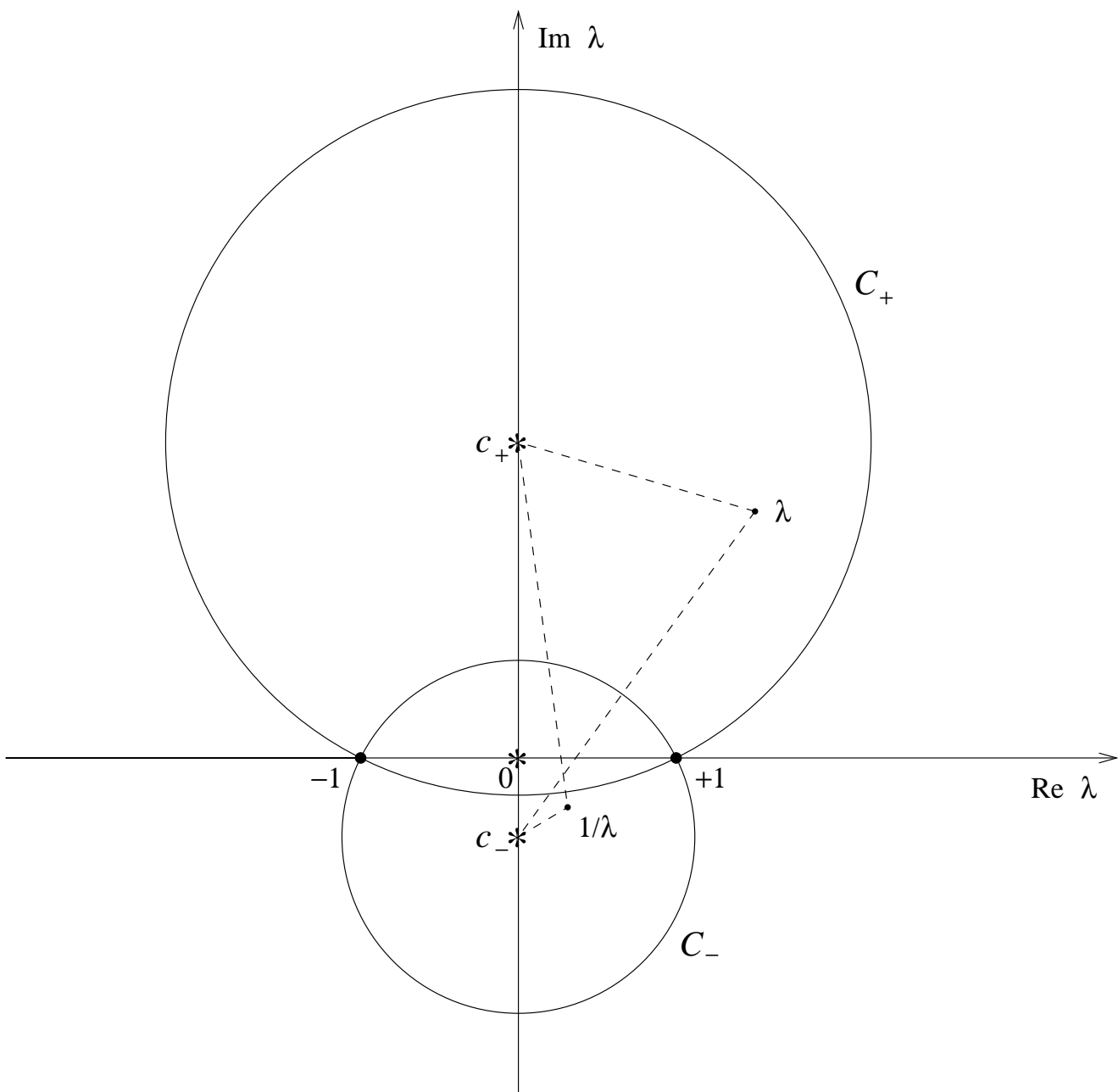


Figure 3:

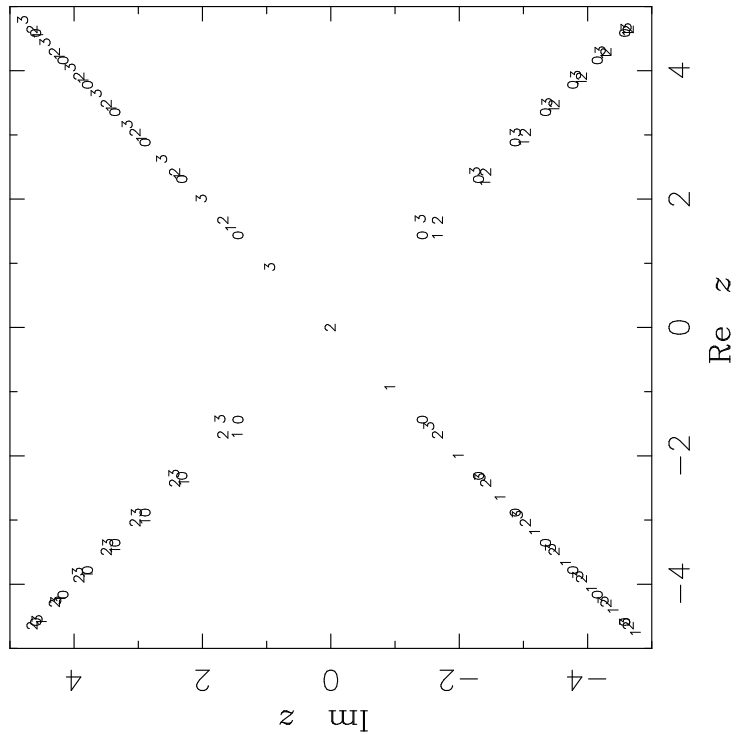
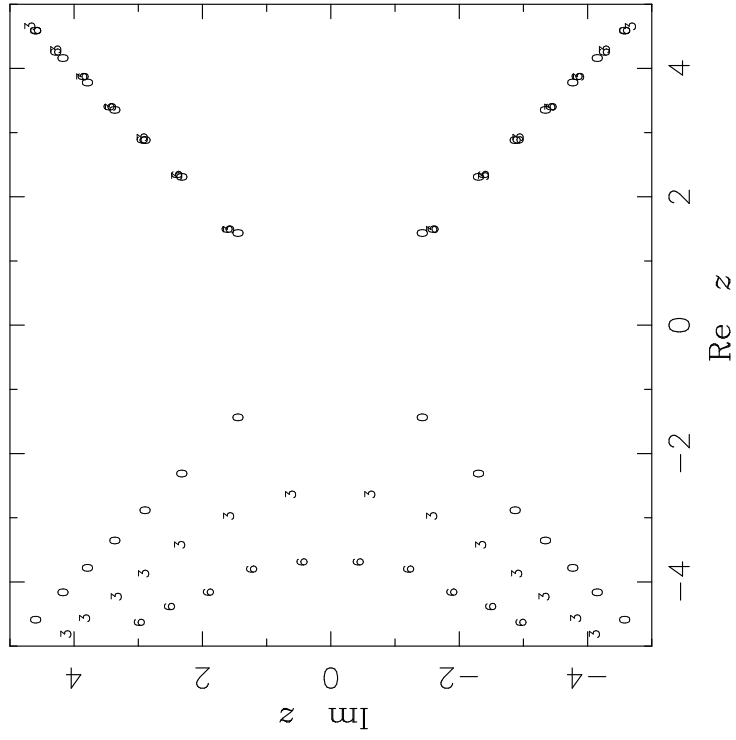


Figure 4:

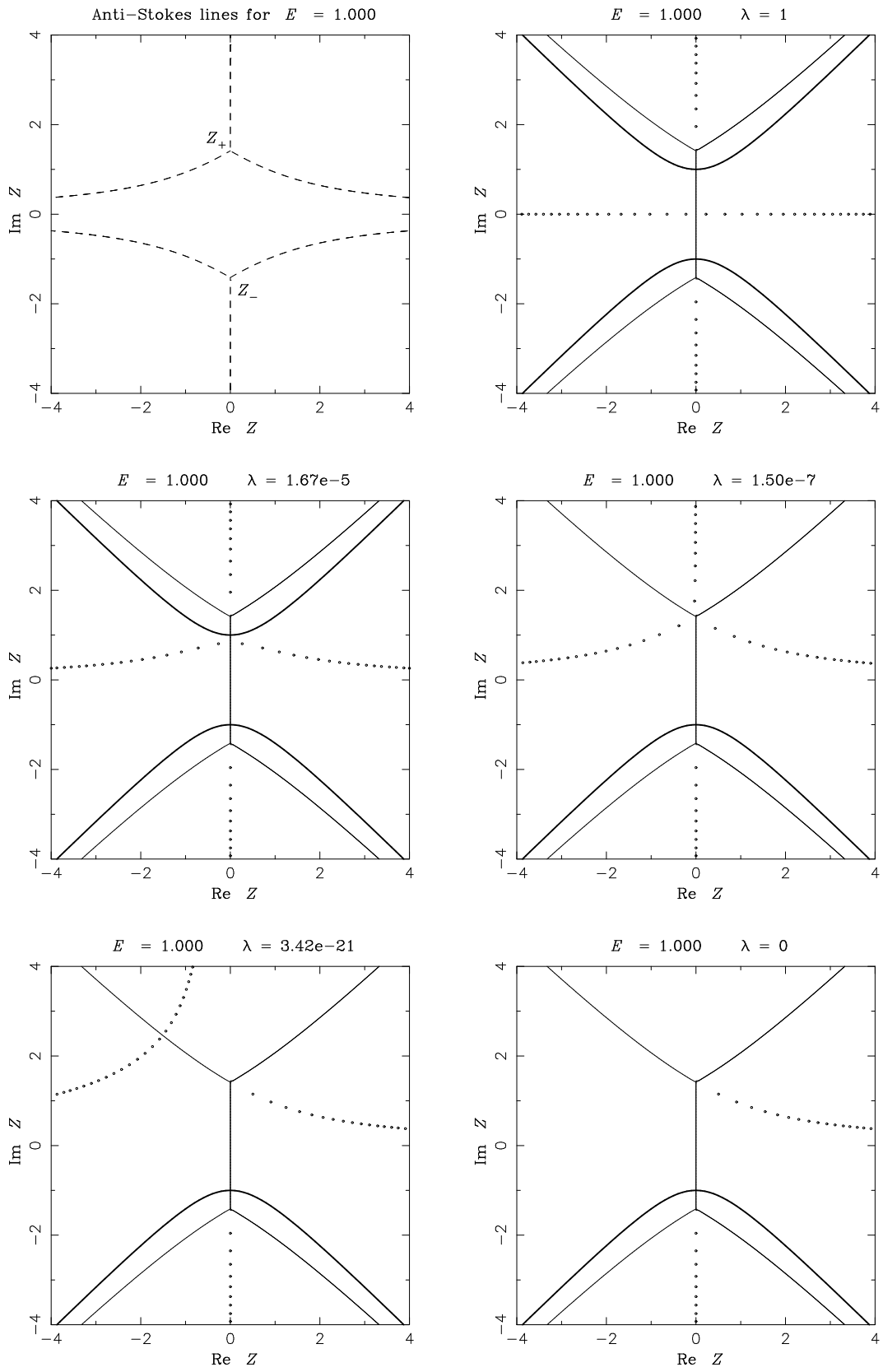


Figure 5:

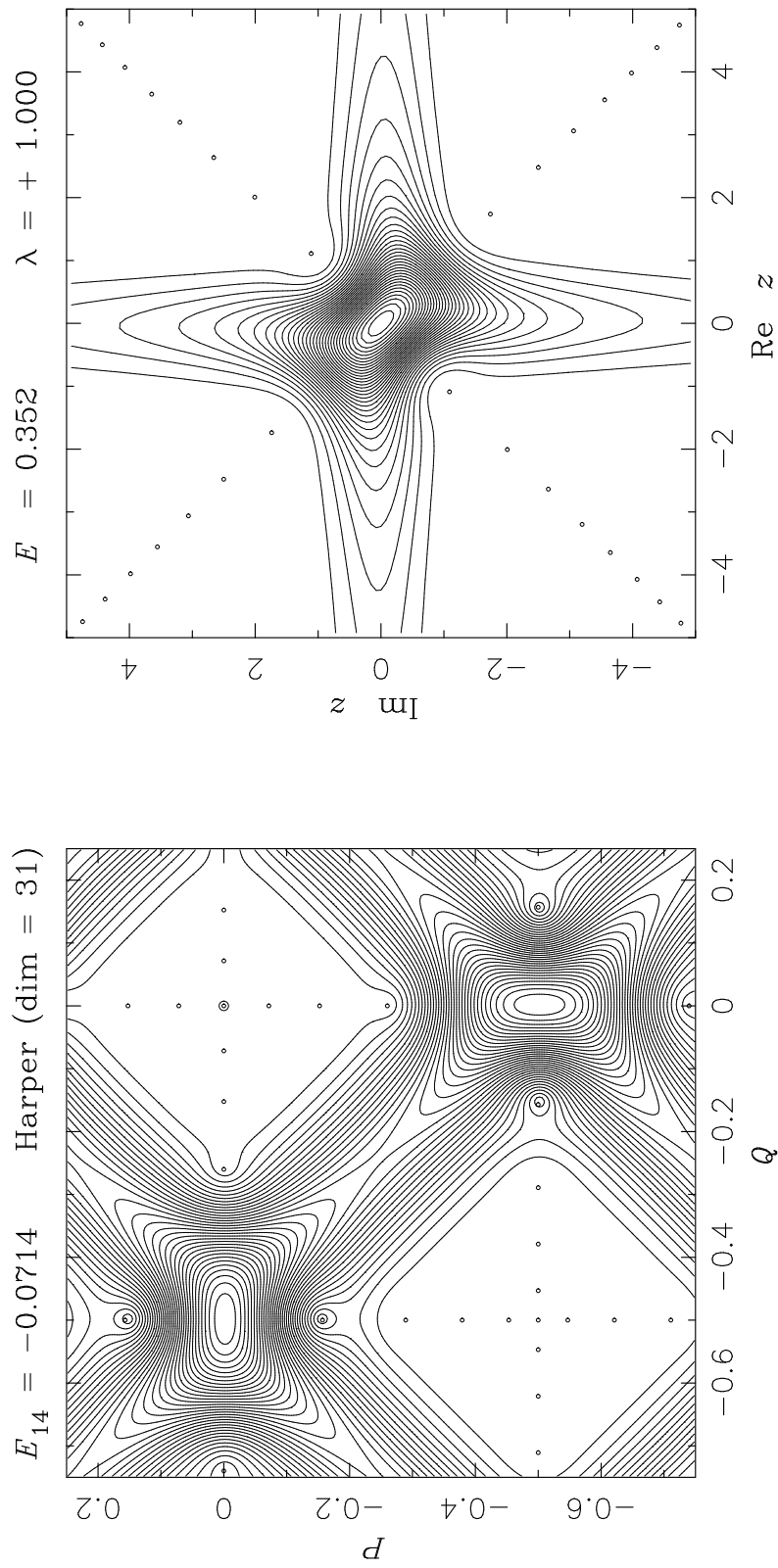


Figure 6: